Biointerface Research in Applied Chemistry
Open-Access Journal (ISSN: 2069-5837)

Article
Volume 13, Issue 5, 2023, 436
https://doi.org/10.33263/BRIAC135.436

A Numerical Study on Unsteady MHD Williamson Nanofluid Flow past a Permeable Moving Cylinder in the presence of Thermal Radiation and Chemical Reaction

Shiva Rao [1,*], Paramananda Deka [1]

[1] Department of Mathematics, Dibrugarh University, Dibrugarh, India
* Correspondence: shivarao374@gmail.com;

Scopus Author ID 57856468200
Received: 7.09.2022; Accepted: 7.10.2022; Published: 19.12.2022

Abstract: The current investigation considers the unsteady two-dimensional MHD flow along with heat and mass transfer of Williamson nanofluid over a moving cylinder of a porous medium. The influence of chemical reactions, thermal radiation, and Joule heating are also considered. This article will use the Buongiorno model to explore the Brownian motion heat transfer process and thermophoresis. The boundary layer governing equations is made non-dimensional by employing the usual transformation. To solve the non-linear dimensionless governing equations, a technique known as the explicit finite difference method (EFDM) is used. A stability analysis was carried out to make the approach more convergent, and an efficient criterion ($Le \geq 0.018$ and $Pr \geq 0.03$) was obtained. The influence of different parameters on the velocity, temperature, and concentration profile are illustrated graphically. From this study, we have achieved that the increase in radiation raises the temperature of the boundary layer region. Also, it was found that the speed of the hybrid nanofluid can be controlled by applying a magnetic field and porous media and enhancing Williamson parameters. To validate the accuracy of the numerical scheme, a qualitative comparison of the results obtained is made with that of the previously published works.

Keywords: Williamson nanofluid; moving cylinder; explicit finite difference method; thermal radiation; chemical reaction; porous medium.

1. Introduction

The remarkable heat transfer characteristics of nanofluid without any pressure drop have attracted a lot of attention from researchers over the past few decades. Conventional fluids have very low thermal conductivity; as a result, they cannot be used for ultra-high cooling processes. Nowadays, nanofluid is used as a base fluid instead of ordinary fluid because of its enhanced thermal properties as compared to ordinary fluid. Nanofluids are made by adding nanoparticles like Ag, Cu, Al_2O_3, etc., into the base fluid like water, ethylene glycol, etc. The idea that dispersing nanoparticles in the base fluid may improve thermal conductivity was first introduced by Choi [1]. After evaluating the thermal conductivity of various metal oxides, Lee *et al*. [2] found that both shape and size contributed significantly to the improved thermal conductivity of the nanofluid. According to the research conducted by Eastman *et al*. [3], the thermal conductivity of ethylene glycol could be increased by as much as 40% if copper nanoparticles (with a volume fraction of less than 1 percent) were added. To explain the enhancement in nanofluid's thermal conductivity, Buongiorno [4] identified Brownian motion

and thermophoresis as two major processes for efficiently increasing the base fluid's thermal conductivity. Nield and Kuznetsov [5] looked into Buongiorno's model to study an incompressible nanofluid flow over a vertical plate. Khan and Pop [6] investigate how the heat transmission and nanoparticle volume fraction change in a nanofluid as it moves down a stretching sheet. The heat transfer characteristics of a nanofluid were studied by Makinde and Aziz [7] across a non-linearly stretching sheet flow subjected to convective boundary conditions. To find a solution to Khan and Pop's problem with the non-linearly stretched sheet, Rana and Bhargava [8] used the FEM method approach.

Due to the wide range of applications, researchers in the area of hydrodynamics have been dedicating their time to studying the issue related to the flow of non-Newtonian fluid over a cylinder for the last few decades. The extrusion process, metal extraction, annealing, thinning of copper wire, and pipe industry are examples of their applications. When it comes to non-Newtonian fluids, the Williamson fluid is among the most important due to its low viscosity at high shear rates. Specifically, the Williamson fluid model predicts that the effective viscosity will fall monotonically with the increase in shear rate and vice versa. This model was first introduced by Williamson [9] in 1929. This pseudoplastic fluid behavior is one example of the many ways in which this non-Newtonian fluid might be put to use in modern industry. For instance, monitoring mass and heat movement between arteries in blood during hemodialysis is important in biological engineering. Unsteady Radiative blood flow of Williamson fluid against a wedge was investigated by Subbarayudu *et al*. [10]. In Zero gravity conditions, Lyubimova *et al*. [11] investigated some important factors on Williamson fluid between two parallel plates. Hashim *et al*. [12] studied the phenomenon of heat transfer of the Williamson nanofluid flow caused by the stretching/shrinking cylinder under a non-uniform magnetic field. Hamid *et al*. [13] later extended the work of Hashim *et al*. by considering the flow caused by an inclined expanding/contracting cylinder and investigating the effect of thermal radiation. Some more detailed work on the Williamson model was discussed in refs. [14-20].

The influence of thermal radiation on free convection has risen in prominence due to its many practical applications in engineering and physics, especially in developing tools and machinery, aerospace engineering, and gas turbines. Regarding heat transfer, thermal radiation is preferable to conduction and convection since it does not need a medium. Because of these characteristics, thermal radiation plays a crucial role in the heat transmission of MHD nanofluids, minimizing heat loss. England and Emery [21] investigated the effect of thermal radiation on Air and CO_2 of laminar flow through the vertical plate. The effect of thermal radiation on unsteady MHD nanofluid flow caused due to a stretching sheet was discussed by Shakhaoath *et al*. [22]. Kumar *et al*. [23] proposed a nanofluid model for flow and heat transmission over an infinite vertical plate with a magnetic field and viscous dissipation. Ali *et al*. [24] studied the impact of thermal radiation and non-uniform heat flux on the MHD hybrid nanofluid flow over the stretching cylinder. In a situation where the bottom plate was permeable and stretchy, Lv *et al*. [25] investigated the impact of thermal radiation, hall current, and uneven heat source/sink on the nanofluid flow between two horizontal flat plates. Recently, Rao and Deka [26] investigated the influence of thermal radiation and chemical reaction on MHD Casson nanofluid flow caused due to a stretching sheet.

The process by which the energy of an electric current is turned into heat when it goes through resistance is referred to as Joule heating (also known as resistive or Ohmic heating). This is because when an electrical current travels through solid or liquid materials that carry current, the electrical energy is transformed into heat energy due to resistances inside the

conductor. Collisions between free electrons transmit energy in this scenario. Ramzan *et al*. [27] investigated the effect of thermal radiation and Joule heating in the MHD micropolar fluid flow, considering the slip condition. Unsteady MHD Jeffery nanofluid flow caused by a vertically stretchable cylinder was studied by Rasheed *et al*. [28], who examined the impact of Joule heating with thermal radiation. The effect of Joule heating with chemical reaction, thermal radiation, and heat generation on three-dimensional Maxwell nanofluid flow was discussed by Ahmad *et al*. [29]. Some recent work on the effect of Joule heating is discussed in refs. [27-35].

To the best of our knowledge, there hasn't been much exploration of the flow and energy transport phenomena of Williamson nanofluid over a vertically permeable moving cylinder. In light of the investigation mentioned above, our present study focuses on the unsteady MHD Williamson nanofluid flow under the presence of thermal radiation, chemical reaction, and Joule heating over a vertical permeable moving cylinder. The governing equations are made dimensionless using the usual transformation, which depends on the magnetic parameter (M), radiation parameter (Rd), Reactive parameter (γ), Prandtl number (Pr), Eckert number (E_c), Grashof number (G_r), modified Grashof number (G_m), Lewis number (Le), Permeability parameter (K_p), Williamson parameter (λ), Brownian motion parameter (Nb), and thermophoresis parameter (Nb). The obtained dimensionless non-linear equations have been solved numerically using an explicit finite difference scheme. The efficiency of the finite difference scheme and the stability analysis of the scheme have been analyzed.

2. Mathematical Model of the Flow

In this study, a two-dimensional unsteady Williamson nanofluid flow past a permeable vertical moving cylinder has been considered under the influence of the magnetic field, thermal radiation, and chemical reaction. Let r_o be the radius of the cylinder, and the x- axis is chosen vertically along the cylinder, whereas the radial coordinate r is chosen normally to the surface. The physical model with the coordinates system of the flow is shown in Figure 1.

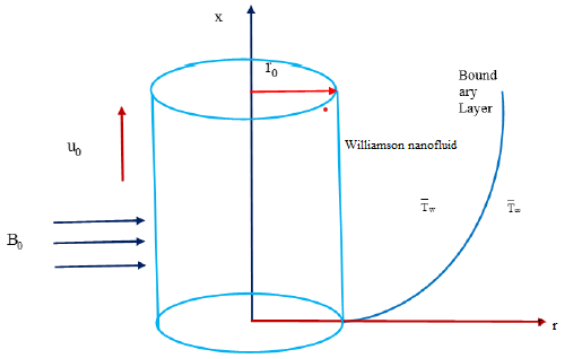

Figure 1. Schematic diagram of the problem.

Let u_o be the velocity at which the cylinder is moving. At time $t > 0$, the temperature and the nanoparticle concentration rose to T_w $(> T_\infty)$ and C_w $(> C_\infty)$ respectively and remained constant thereafter, where T_w, C_w are the temperature and nanoparticle concentration at the cylinder surface, and T_∞, C_∞ are the temperature and nanoparticle concentration far away from the surface, respectively. An external uniform magnetic field B_o is applied to the cylindrical surface along the direction normal to x-axis. Considering that the fluid is slightly

conducting, the magnetic Reynolds number is much less than unity; thus, the induced magnetic field is negligible compared to the applied magnetic field.

For the Williamson fluid model [9], Cauchy stress tensor S can be expressed as:

$$S = -pI + \bar{\tau} \quad \ldots(1)$$

$$\bar{\tau} = \left[\mu_\infty + \frac{\mu_o - \mu_\infty}{1 - \Gamma\gamma^*}\right] A_1 \quad \ldots(2)$$

Here, γ^* is defined as:

$$\gamma^* = \left(\frac{\pi}{2}\right)^{\frac{1}{2}}, where\ \pi = \ trace(A_1)^2 \quad \ldots(3)$$

Considering the case for $\mu_\infty = 0$ and $\Gamma\gamma^* < 1$, Equation (2) becomes:

$$\bar{\tau} = \left[\frac{\mu_o}{1 - \Gamma\gamma^*}\right] A_1$$

By using binomial expansion, we get:

$$\bar{\tau} = \mu_o(1 + \Gamma\gamma^*)A_1 \quad \ldots(4)$$

The governing equations of the nanofluid may be expressed in vector form using the Cartesian coordinates x and y as -

The Continuity Equation:

$$\nabla.\vec{q} = 0 \quad \ldots(5)$$

The Momentum Equation:

$$\rho\left[\frac{\partial\vec{q}}{\partial t} + (\vec{q}.\nabla)\vec{q}\right] = -\nabla p + \mu\nabla^2\vec{q} - \vec{J}\times\vec{B} + \vec{g}\beta_t(\bar{T} - \bar{T}_\infty) + \vec{g}\beta_c(\bar{C} - \bar{C}_\infty) - \left(\frac{\mu}{k_0}\right)\vec{q} \quad \ldots(6)$$

Ohm's law

$$\vec{J} = \sigma[\vec{E} + (\vec{q}\times\vec{B})] \quad \ldots(7)$$

Gauss law of magnetism

$$\nabla.\vec{B} = 0 \quad \ldots(8)$$

The Energy Equation:

$$\rho C_p\left[\frac{\partial \bar{T}}{\partial t}+(\vec{q}.\nabla)\bar{T}\right] = \kappa\nabla^2\bar{T}+\mu\,(\nabla\vec{q}.\nabla\vec{q})-\nabla q_r+\left(\vec{J}\times\vec{B}\right)q^2 + \rho C_p\left[D_B(\nabla\bar{C}.\nabla\bar{T})+\left(\frac{D_T}{\bar{T}_\infty}\right)(\nabla\bar{T}.\nabla\bar{T})\right] \quad \ldots(9)$$

The Concentration Equation:

$$\frac{\partial \bar{C}}{\partial t}+(\vec{q}.\nabla)\bar{C}=D_B\nabla^2\bar{C}+\frac{D_T}{\bar{T}_\infty}\nabla^2\bar{T}-K_1(\bar{C}-\bar{C}_\infty) \quad \ldots(10)$$

Here we consider $\vec{q}$ is a function of u and v.

The following equations describe the unsteady MHD Williamson nanofluid flow with heat and mass transfer under the aforementioned assumptions and under standard boundary conditions. [36-38]:

The Continuity Equation:

$$\frac{\partial(ru)}{\partial x}+\frac{\partial(rv)}{\partial r}=0 \quad \ldots(11)$$

The Momentum Equation:

$$\frac{\partial u}{\partial t}+u\frac{\partial u}{\partial x}+v\frac{\partial v}{\partial r} = \nu\left(\frac{\partial^2 u}{\partial r^2}+\frac{1}{r}\frac{\partial u}{\partial r}\right)+\sqrt{2}\nu\Gamma\frac{\partial u}{\partial r}\left(\frac{\partial^2 u}{\partial r^2}+\frac{1}{r}\frac{\partial u}{\partial r}\right)+g\beta_t(\bar{T}-\bar{T}_\infty) + g\beta_c(\bar{C}-\bar{C}_\infty)-\frac{\sigma_e B_o^2}{\rho}u-\frac{\nu}{k_o}u \quad \ldots(12)$$

The Energy Equation:

$$\frac{\partial \bar{T}}{\partial t}+u\frac{\partial \bar{T}}{\partial x}+v\frac{\partial \bar{T}}{\partial r} = \frac{\kappa}{\rho C_p}\left(\frac{\partial^2\bar{T}}{\partial r^2}+\frac{1}{r}\frac{\partial \bar{T}}{\partial r}\right)+\frac{\sigma_e B_o^2}{\rho C_p}u^2+\tau^*\left\{D_B\left(\frac{\partial \bar{C}}{\partial r}\frac{\partial \bar{T}}{\partial r}\right)+\frac{D_T}{T_\infty}\left(\frac{\partial \bar{T}}{\partial r}\right)^2\right\} - \frac{1}{\rho C_p}\frac{\partial q_r}{\partial r} \quad \ldots(13)$$

The Concentration Equation:

$$\frac{\partial \bar{C}}{\partial t}+u\frac{\partial \bar{C}}{\partial x}+v\frac{\partial \bar{C}}{\partial r}=D_B\left(\frac{\partial^2\bar{C}}{\partial r^2}+\frac{1}{r}\frac{\partial \bar{C}}{\partial r}\right)+\frac{D_T}{T_\infty}\left(\frac{\partial^2\bar{T}}{\partial r^2}+\frac{1}{r}\frac{\partial \bar{T}}{\partial r}\right)-K_1(\bar{C}-\bar{C}_\infty) \quad \ldots(14)$$

The initial and boundary conditions are as follows:

$t \leq 0 \quad u = 0 \quad v = 0 \quad \bar{T} = \bar{T}_\infty \quad \bar{C} = \bar{C}_\infty \quad$ for all $x \geq 0$ and $r \geq 0$

$t > 0 \quad u = u_o \quad v = 0 \quad \bar{T} = \bar{T}_w \quad \bar{C} = \bar{C}_w \quad$ at $r = r_o$

$u = 0 \quad v = 0 \quad \bar{T} = \bar{T}_\infty \quad \bar{C} = \bar{C}_\infty \quad$ at $x = 0$ and $r \geq r_o$

$u \to 0 \quad \bar{T} \to \bar{T}_\infty \quad \bar{C} \to \bar{C}_\infty \quad as\ r \to \infty$ ...(15)

Rosseland approximation allows us to write the radiative heat flux term q_r as [39-41]:

$$q_r = \frac{-4\sigma^*}{3k^*}\frac{\partial \bar{T}^4}{\partial r} \quad \ldots(16)$$

If we generalise the Taylor series and exclude the higher order terms, we obtain

$$\bar{\mathrm{T}}^4 = 4\,\bar{\mathrm{T}}_\infty^3\,\bar{\mathrm{T}} - 3\,\bar{\mathrm{T}}_\infty^4$$

Hence eq. (16) becomes-

$$\frac{\partial q_r}{\partial r} = -\frac{16\sigma^*\bar{T}_\infty^3}{3k^*}\frac{\partial^2 \bar{T}}{\partial r^2} \quad \ldots(17)$$

Introducing the dimensionless variable [42]:

$$U = \frac{u}{U_o}, \quad V = \frac{vr_o}{\nu}, \quad X = \frac{x\nu}{U_o r_o^2}, \quad R = \frac{r}{r_o}, \quad \tau = \frac{t\nu}{r_o^2}, \quad \ldots(18)$$

$$T = \frac{\bar{T} - \bar{T}_\infty}{\bar{T}_w - \bar{T}_\infty}, \quad C = \frac{\bar{C} - \bar{C}_\infty}{\bar{C}_w - \bar{C}_\infty}$$

Then eqns. (11) to (14) becomes:

$$\frac{\partial (RU)}{\partial X} + \frac{\partial (RV)}{\partial R} = 0 \quad \ldots(19)$$

$$\frac{\partial U}{\partial \tau} + U\frac{\partial U}{\partial X} + V\frac{\partial U}{\partial R} = \left(1 + \lambda\frac{\partial U}{\partial R}\right)\left(\frac{\partial^2 U}{\partial R^2} + \frac{1}{R}\frac{\partial U}{\partial R}\right) + G_r T + G_m C - (M + K_p)U \quad \ldots(20)$$

$$\frac{\partial T}{\partial \tau} + U\frac{\partial T}{\partial X} + V\frac{\partial T}{\partial R} = \frac{1}{Pr}\,(1 + Rd)\left(\frac{\partial^2 T}{\partial R^2} + \frac{1}{R}\frac{\partial T}{\partial R}\right) + Nb\frac{\partial C}{\partial R}\frac{\partial T}{\partial R} + Nt\left(\frac{\partial T}{\partial R}\right)^2 + ME_c U^2 \quad \ldots(21)$$

$$\frac{\partial C}{\partial \tau} + U\frac{\partial C}{\partial X} + V\frac{\partial C}{\partial R} = \frac{1}{Le}\left[\left(\frac{\partial^2 C}{\partial R^2} + \frac{1}{R}\frac{\partial C}{\partial R}\right) + \frac{Nt}{Nb}\left(\frac{\partial^2 T}{\partial R^2} + \frac{1}{R}\frac{\partial T}{\partial R}\right)\right] - \gamma C \quad \ldots(22)$$

The dimensionless boundary conditions are:

$$\tau \le 0, \quad U = 0, \quad V = 0, \quad T = 0, \quad C = 0 \qquad everywhere$$

$$\tau \le 0, \quad U = 0, \quad V = 0, \quad T = 0, \quad C = 0 \qquad everywhere$$

$$\tau > 0, \quad U = 1, \quad V = 0, \quad T = 1, \quad C = 1 \qquad at\ R = 1$$

$$U = 0, \quad V = 0, \quad T = 0, \quad C = 0 \qquad at\ X = 0 \text{ and } R \ge 1$$

$$U \to 0, \quad V \to 0, \quad T \to 0, \quad C \to 0 \qquad as\ R \to \infty \qquad ...(23)$$

In this study, we specify the flow parameters as follows: -

$$\lambda = \frac{\sqrt{2}\Gamma U_o}{r_o} \qquad M = \frac{\sigma_e B_o^2 r_o^2}{\rho\nu} \qquad G_r = \frac{g\beta_t(\bar{T}_w - \bar{T}_\infty)\nu}{U_o^3} \qquad G_m = \frac{g\beta_c(\bar{C}_w - \bar{C}_\infty)\nu}{U_o^3}$$

$$K_p = \frac{r_o^2}{k_o} \qquad Ec = \frac{U_o^2}{C_p(\bar{T}_w - \bar{T}_\infty)} \qquad Pr = \frac{\nu\rho C_p}{\kappa} \qquad Rd = \frac{16\sigma^*\bar{T}_\infty^3}{3\kappa\kappa^*}$$

$$N_b = \frac{\tau D_B(\bar{C}_w - \bar{C}_\infty)}{\nu} \qquad Nt = \frac{\tau D_T(\bar{T}_w - \bar{T}_\infty)}{\bar{T}_\infty\nu} \qquad Le = \frac{\nu}{D_B} \qquad \gamma = \frac{\nu K_p}{r_o^2}$$

3. Numerical Procedure

An explicit finite differential system of equations is developed for solving the non-linear coupled partial differential equations (16) – (19) under the boundary conditions of Equation (20).

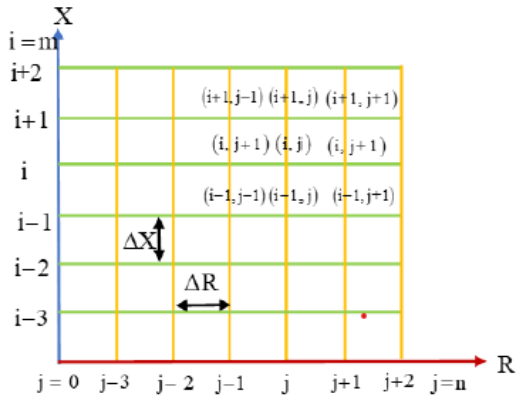

Figure 2. Finite difference space grid.

The flow field is considered a rectangular area, and grid lines are lines parallel to both X and R direction, with the X direction running parallel to the cylinder and the Y direction running normally to the vertical cylinder. The height of the cylinder is considered to be in the range [0,20]. Therefore, X may be any positive integer, and the radius, R, can be any positive real number from [0,50]. Figure 2 depicts a space grid with m=100 nodes along the X-axis and n=200 nodes along the R-axis.

The subscripts i and j denote the grid points toward the X and R coordinates, respectively, where $X = i\Delta X$ and $R = 1 + (j-1)\Delta R$. Additionally, the values of U, V, T, and C at the end of a time step may be assumed to be U', V', T', and C'. In order to derive the following sets of finite difference equations, an explicit finite difference technique is used:

$$\frac{U_{i,j} - U_{i-1,j}}{\Delta X} + \frac{V_{i,j} - V_{i,j-1}}{\Delta R} + \frac{V_{i,j}}{1 + (j-1)\Delta R} = 0 \quad \ldots(24)$$

$$\frac{U'_{i,j} - U_{i,j}}{\Delta \tau} + U_{i,j}\frac{U_{i,j} - U_{i-1,j}}{\Delta X} + V_{i,j}\frac{U_{i,j+1} - U_{i,j}}{\Delta R} = \left(1 + \lambda \frac{U_{i,j+1} - U_{i,j}}{\Delta R}\right)\left(\frac{U_{i,j+1} - 2U_{i,j} + U_{i,j-1}}{(\Delta R)^2} + \frac{1}{1 + (j-1)\Delta R}\frac{U_{i,j+1} - U_{i,j}}{\Delta R}\right) + + G_r T_{i,j} + G_m C_{i,j} - (K_p + M)U_{i,j} \quad \ldots(25)$$

$$\frac{T'_{i,j} - T_{i,j}}{\Delta \tau} + U_{i,j}\frac{T_{i,j} - T_{i-1,j}}{\Delta X} + V_{i,j}\frac{T_{i,j+1} - T_{i,j}}{\Delta R} = \left(\frac{1 + Rd}{Pr}\right)\left(\frac{T_{i,j+1} - 2T_{i,j} + T_{i,j-1}}{(\Delta R)^2} + \frac{1}{1 + (j-1)\Delta R}\frac{T_{i,j+1} - T_{i,j}}{\Delta R}\right) + Nb\left(\frac{T_{i,j+1} - T_{i,j}}{\Delta R}\frac{C_{i,j+1} - C_{i,j}}{\Delta R}\right) + Nt\left(\frac{T_{i,j+1} - T_{i,j}}{\Delta R}\right)^2 + ME_c U_{i,j}^2 \quad \ldots(26)$$

$$\frac{C'_{i,j} - C_{i,j}}{\Delta \tau} + U_{i,j}\frac{C_{i,j} - C_{i-1,j}}{\Delta X} + V_{i,j}\frac{C_{i,j+1} - C_{i,j}}{\Delta R} = \frac{1}{Le}\left[\left(\frac{C_{i,j+1} - 2C_{i,j} + C_{i,j-1}}{(\Delta R)^2} + \frac{1}{1 + (j-1)\Delta R}\frac{C_{i,j+1} - C_{i,j}}{\Delta R}\right) + \frac{Nt}{Nb}\left(\frac{T_{i,j+1} - 2T_{i,j} + T_{i,j-1}}{(\Delta R)^2} + \frac{1}{1 + (j-1)\Delta R}\frac{T_{i,j+1} - T_{i,j}}{\Delta R}\right)\right] - \gamma C_{i,j} \quad \ldots(27)$$

Along with initial and boundary conditions:

when, $t \leq 0$ then $U_{0,j} = 0,\ V_{0,j} = 0,\ T_{0,j} = 0,\ C_{0,j} = 0$ everywhere

when, $t > 0$ then $U_{0,j} = 1,\ V_{0,j} = 0,\ T_{0,j} = 1,\ C_{0,j} = 1$ for all $R = 1$

$U_{n,j} = 0,\ V_{n,j} = 0,\ T_{n,j} = 0,\ C_{n,j} = 0$ as $R \to \infty$ …(28)

where the superscript n denotes the value of time, $\tau = n.\Delta\tau$ where n=1, 2, 3, 4..., and the i and j represent the grid points with X and Y coordinates, respectively. Each mesh size is maintained constant in the x and y directions at X=0.202 and Y=0.251 with a smaller time step of τ=0.0005.

4. Stability and Convergence Analysis

Since the implementation of the finite difference is explicit, it is crucial to address the stability and convergence analysis of the issue. Equation (21) is overpassed since $\Delta\tau$ is absent from it. Apart from the constants, the Fourier expansion of U, T, and C is often written as $e^{i\alpha X}e^{i\beta Y}$ for any time $\tau = 0$. Here $i = \sqrt{-1}$. The following equations are attainable at time t:

$$\left.\begin{aligned} &U: \psi(\tau)e^{i\alpha X}e^{i\beta R} \\ &T: \theta(\tau)e^{i\alpha X}e^{i\beta R} \\ &C: \phi(\tau)e^{i\alpha X}e^{i\beta R} \end{aligned}\right\} \ldots(29)$$

$$\left.\begin{aligned} &U': \psi'(\tau)e^{i\alpha X}e^{i\beta R} \\ &T': \theta'(\tau)e^{i\alpha X}e^{i\beta R} \\ &C': \phi'(\tau)e^{i\alpha X}e^{i\beta R} \end{aligned}\right\} \ldots(30)$$

Substituting Eqns. (29) and (30) into Eqns. (25) - (27), we get:

Momentum Equation:

$$\begin{aligned} &\frac{\left(\psi'(\tau)-\psi(\tau)\right)e^{i\alpha X}e^{i\beta R}}{\Delta\tau} + U\psi(\tau)\frac{\left(1-e^{-i\alpha\Delta X}\right)e^{i\alpha X}e^{i\beta R}}{\Delta X} + V\psi(\tau)\frac{\left(e^{i\beta\Delta R}-1\right)e^{i\alpha X}e^{i\beta R}}{\Delta R} \\ &= \left(1+\lambda\psi(\tau)\frac{\left(e^{i\beta\Delta R}-1\right)e^{i\alpha X}e^{i\beta R}}{\Delta R}\right)\left(\psi(\tau)\frac{2(cos\beta\Delta R)-1)e^{i\alpha X}e^{i\beta R}}{(\Delta R)^2}\right. \\ &\left.+\frac{\psi(\tau)}{R}\frac{\left(e^{i\beta\Delta R}-1\right)e^{i\alpha X}e^{i\beta R}}{\Delta R}\right) + G_r\theta(\tau)e^{i\alpha X}e^{i\beta R} + G_m\phi(\tau)e^{i\alpha X}e^{i\beta R} - (M \\ &+ K_p)\psi(\tau)e^{i\alpha X}e^{i\beta R} \\ \Rightarrow\ &\psi'(\tau) = \psi(\tau)\left[1 - U\Delta\tau\frac{\left(1-e^{-i\alpha\Delta X}\right)}{\Delta X} - V\Delta\tau\frac{\left(e^{i\beta\Delta R}-1\right)}{\Delta R}\right. \\ &+\left(1+U\lambda\frac{\left(e^{i\beta\Delta R}-1\right)}{\Delta R}\right)\left(\frac{2\Delta\tau(cos\beta\Delta R)-1)}{(\Delta R)^2}\right. \\ &\left.\left.+\frac{\Delta\tau}{R}\frac{\left(e^{i\beta\Delta R}-1\right)}{\Delta R}\right) - \left(M+K_p\right)\Delta\tau\right] + G_r\Delta\tau\theta(\tau) \\ &+ G_m\Delta\tau\phi(\tau) \end{aligned} \quad \ldots(31)$$

Energy Equation:

$$\begin{aligned} &\frac{(\theta'(\tau)-\theta(\tau))e^{i\alpha X}e^{i\beta R}}{\Delta\tau} + U\theta(\tau)\frac{\left(1-e^{-i\alpha\Delta X}\right)e^{i\alpha X}e^{i\beta R}}{\Delta X} + V\theta(\tau)\frac{\left(e^{i\beta\Delta R}-1\right)e^{i\alpha X}e^{i\beta R}}{\Delta R} \\ &= \left(\frac{1+R}{Pr}\right)\left(\theta(\tau)\frac{2(cos\beta\Delta R)-1)e^{i\alpha X}e^{i\beta R}}{(\Delta R)^2} + \frac{\theta(\tau)}{R}\frac{\left(e^{i\beta\Delta R}-1\right)e^{i\alpha X}e^{i\beta R}}{\Delta R}\right) \\ &+ NbC\theta(\tau)\left(\frac{e^{i\beta\Delta R}-1}{\Delta R}\right)^2 + NtT\theta(\tau)\left(\frac{e^{i\beta\Delta R}-1}{\Delta R}\right)^2 + ME_cU\psi(\tau)e^{i\alpha X}e^{i\beta R} \end{aligned}$$

$$\Rightarrow \theta'(\tau) = \theta(\tau)\left[1 - U\Delta\tau\frac{\left(1-e^{-i\alpha\Delta X}\right)}{\Delta X} - V\Delta\tau\frac{\left(e^{i\beta\Delta R}-1\right)}{\Delta R}\right. \quad \ldots(32)$$
$$+\left(\frac{1+Rd}{Pr}\right)\left(\frac{2\Delta\tau(cos\beta\Delta R)-1)}{(\Delta R)^2}+\frac{\Delta\tau}{R}\frac{\left(e^{i\beta\Delta R}-1\right)}{\Delta R}\right)$$
$$\left.+NbC\Delta\tau\left(\frac{e^{i\beta\Delta R}-1}{\Delta R}\right)^2+NtT\Delta\tau\left(\frac{e^{i\beta\Delta R}-1}{\Delta R}\right)^2\right]$$
$$+ME_cU\Delta\tau\psi(\tau)$$

Concentration Equation:

$$\frac{(\phi'(\tau)-\phi(\tau))e^{i\alpha X}e^{i\beta R}}{\Delta\tau}+U\phi(\tau)\frac{\left(1-e^{-i\alpha\Delta X}\right)e^{i\alpha X}e^{i\beta R}}{\Delta X}+V\phi(\tau)\frac{\left(e^{i\beta\Delta Y}-1\right)e^{i\alpha X}e^{i\beta R}}{\Delta R}$$
$$=\frac{1}{Le}\left[\left(\phi(\tau)\frac{2(cos\beta\Delta R)-1)e^{i\alpha X}e^{i\beta R}}{(\Delta R)^2}+\frac{\phi(\tau)}{R}\frac{\left(e^{i\beta\Delta R}-1\right)e^{i\alpha X}e^{i\beta R}}{\Delta R}\right)\right.$$
$$\left.+\frac{Nt}{Nb}\left(\theta(\tau)\frac{2(cos\beta\Delta R)-1)e^{i\alpha X}e^{i\beta R}}{(\Delta R)^2}+\frac{\theta(\tau)}{R}\frac{\left(e^{i\beta\Delta R}-1\right)e^{i\alpha X}e^{i\beta R}}{\Delta R}\right)\right]$$
$$-\gamma\phi(\tau)e^{i\alpha X}e^{i\beta R}$$

$$\Rightarrow \phi'(\tau) = \phi(\tau)\left[1 - U\Delta\tau\frac{\left(1-e^{-i\alpha\Delta X}\right)}{\Delta X} - V\Delta\tau\frac{\left(e^{i\beta\Delta R}-1\right)}{\Delta R}\right. \quad \ldots(33)$$
$$\left.+\frac{1}{Le}\left(\frac{2\Delta\tau(cos\beta\Delta R)-1)}{(\Delta R)^2}+\frac{\Delta\tau}{R}\frac{\left(e^{i\beta\Delta R}-1\right)}{\Delta R}\right)-\gamma\Delta\tau\right]$$
$$+\theta(\tau)\left[\frac{Nt}{Nb}\left(\frac{2\Delta\tau(cos\beta\Delta R)-1)}{(\Delta R)^2}+\frac{\Delta\tau}{R}\frac{\left(e^{i\beta\Delta R}-1\right)}{\Delta R}\right)\right]$$

Eqn. (25) to (27) can be written in the following form:

$$\psi' = A_1\psi + A_2\theta + A_3\phi \quad \ldots(34)$$
$$\theta' = B\theta + E\psi \quad \ldots(35)$$
$$\phi' = J\phi + K\theta \quad \ldots(36)$$

where

$$A_1 = 1 - U\Delta\tau\frac{\left(1-e^{-i\alpha\Delta X}\right)}{\Delta X} - V\Delta\tau\frac{\left(e^{i\beta\Delta R}-1\right)}{\Delta R}$$
$$+\left(1+U\lambda\frac{\left(e^{i\beta\Delta R}-1\right)}{\Delta R}\right)\left(\frac{2\Delta\tau(cos\beta\Delta R)-1)}{(\Delta R)^2}+\frac{\Delta\tau}{R}\frac{\left(e^{i\beta\Delta R}-1\right)}{\Delta R}\right)$$
$$-\left(M+K_p\right)\Delta\tau$$

$$A_2 = G_r\Delta\tau$$
$$A_3 = G_m\Delta\tau$$

$$B = 1 - U\Delta\tau\frac{\left(1-e^{-i\alpha\Delta X}\right)}{\Delta X} - V\Delta\tau\frac{\left(e^{i\beta\Delta R}-1\right)}{\Delta R}$$
$$+\left(\frac{1+Rd}{Pr}\right)\left(\frac{2\Delta\tau(cos\beta\Delta R)-1)}{(\Delta R)^2}+\frac{\Delta\tau}{R}\frac{\left(e^{i\beta\Delta R}-1\right)}{\Delta R}\right)+NbC\Delta\tau\left(\frac{e^{i\beta\Delta R}-1}{\Delta R}\right)^2$$
$$+NtT\Delta\tau\left(\frac{e^{i\beta\Delta R}-1}{\Delta R}\right)^2$$

$$E = ME_cU\Delta\tau$$

$$J = 1 - U\Delta\tau\frac{\left(1-e^{-i\alpha\Delta X}\right)}{\Delta X} - V\Delta\tau\frac{\left(e^{i\beta\Delta R}-1\right)}{\Delta R} + \frac{1}{Le}\left(\frac{2\Delta\tau(cos\beta\Delta R)-1)}{(\Delta R)^2} + \frac{\Delta\tau}{R}\frac{\left(e^{i\beta\Delta R}-1\right)}{\Delta R}\right) - \gamma\Delta\tau$$

$$K = \frac{Nt}{Nb}\left(\frac{2\Delta\tau(cos\beta\Delta R)-1)}{(\Delta R)^2} + \frac{\Delta\tau}{R}\frac{\left(e^{i\beta\Delta R}-1\right)}{\Delta R}\right)$$

Now Eqn. (34) to (36) can be expressed in matrix form as:

$$\begin{bmatrix}\psi'\\ \theta'\\ \phi'\end{bmatrix} = \begin{bmatrix}A_1 & A_2 & A_3\\ E & B & 0\\ 0 & K & J\end{bmatrix}\begin{bmatrix}\psi\\ \theta\\ \phi\end{bmatrix}$$

$$\Rightarrow \eta' = T\eta$$

where $\eta' = \begin{bmatrix}\psi'\\ \theta'\\ \phi'\end{bmatrix}$, $T = \begin{bmatrix}A_1 & A_2 & A_3\\ E & B & 0\\ 0 & K & J\end{bmatrix}$ and $\eta = \begin{bmatrix}\psi\\ \theta\\ \phi\end{bmatrix}$

Finding the stability condition requires determining the eigen values of the matrix T, which is challenging in this investigation since each element of T is unique. A temporal step-size of zero, or very close to it, i.e., $\Delta\tau \to 0$ is being examined as a potential solution to this issue. This results in $E \to 0$ and $K \to 0$. This leads to the following amplification matrix:

$$T = \begin{bmatrix}A_1 & A_2 & A_3\\ 0 & B & 0\\ 0 & 0 & J\end{bmatrix}$$

Consequently, the eigenvalues of the amplified matrix T are $\lambda_1 = A_1$, $\lambda_2 = B$ and $\lambda_3 = J$.

The modulus of the eigenvalues must not be more than unity for stability. The stability criteria are thus:

$$|A_1| \le 1, \qquad |B| \le 1 \qquad and \qquad |J| \le 1$$

Assuming U is non-negative, and V is non-positive everywhere and choosing $a = \frac{\Delta\tau}{R\Delta R}$, $b = U\frac{\Delta\tau}{\Delta X}$, $c = |-V|\frac{\Delta\tau}{\Delta R}$, $d = \Delta\tau$ and $e = \frac{2\Delta\tau}{(\Delta R)^2}$, where $a, b, c,$ and d are real and non-negative numbers, we have:

$$A_1 = 1 - b\left(1-e^{-i\alpha\Delta X}\right) + c\left(e^{i\beta\Delta R}-1\right) + \left(1 + U\lambda\frac{\left(e^{i\beta\Delta R}-1\right)}{\Delta R}\right)\left(e(cos\beta\Delta R)-1) + a\left(e^{i\beta\Delta R}-1\right)\right) - \left(M + K_p\right)d$$

$$B = 1 - b\left(1-e^{-i\alpha\Delta X}\right) + c\left(e^{i\beta\Delta R}-1\right) + \left(\frac{1+Rd}{Pr}\right)\left(e(cos\beta\Delta R)-1) + a\left(e^{i\beta\Delta R}-1\right)\right) + \frac{NbC\left(e^{i\beta\Delta R}-1\right)^2 e}{2} + \frac{NtT\left(e^{i\beta\Delta R}-1\right)^2 e}{2}$$

$$J = 1 - b\left(1-e^{-i\alpha\Delta X}\right) + c\left(e^{i\beta\Delta R}-1\right) + \frac{1}{Le}\left(e(cos\beta\Delta R)-1) + a\left(e^{i\beta\Delta R}-1\right)\right) - \gamma d$$

When $\alpha\Delta X = m\pi$ and $\beta\Delta Y = n\pi$, where $m = n =$odd integer, the modulus of A_1, B, and J are maximized. Consequently, we have:

$$A_1 = 1 - 2\left[b + c + \left(1 - \frac{2\lambda U}{R}\right)(e + a) + \left(M + K_p\right)d\right]$$

$$B = 1 - 2\left[b + c + \frac{1+Rd}{Pr}(e + a) - (NbC + NtT)e\right]$$

$$C = 1 - 2\left[b + c + \frac{1}{Le}(e + a) + \frac{\gamma d}{2}\right]$$

The highest negative value of A_1, B and J that may be permitted is -1, i.e., $A, B \text{ and } J \geq -1$. This gives:

$$b + c + \frac{1 + Rd}{Pr}(e + a) - (NbC + NtT)e \leq 1$$

$$b + c + \frac{1}{Le}(e + a) + \frac{\gamma d}{2} \leq 1$$

i.e.,

$$U\frac{\Delta\tau}{\Delta X} + |V|\frac{\Delta\tau}{\Delta Y} + \frac{1 + Rd}{Pr}\left(\frac{2\Delta\tau}{(\Delta R)^2} + \frac{\Delta\tau}{R\Delta R}\right) - (NbC + NtT)\frac{2\Delta\tau}{(\Delta R)^2} \leq 1$$

$$U\frac{\Delta\tau}{\Delta X} + |V|\frac{\Delta\tau}{\Delta Y} + \frac{1}{Le}\left(\frac{2\Delta\tau}{(\Delta R)^2} + \frac{\Delta\tau}{R\Delta R}\right) + \frac{\gamma\Delta\tau}{2} \leq 1$$

From the initial condition, we have $U = V = \bar{T} = \bar{C} = 0$ at $\tau = 0$ and we consider $E_c << 1$ and $R \geq 0.5$. Hence, the convergence criteria of the method are $Le \geq 0.018$ and $Pr \geq 0.03$ when $\Delta X = 0.202$, $\Delta R = 0.251$, and $\Delta\tau = 0.0005$.

5. Results and Discussion

The current study's findings are provided in graphical form to analyze the physical representation of the problem. The graphs depict the influence of various factors on the velocity, temperature, and concentration profiles. All the graphs in this study are obtained using the MATLAB program, which implements the explicit finite difference technique to solve the problem.

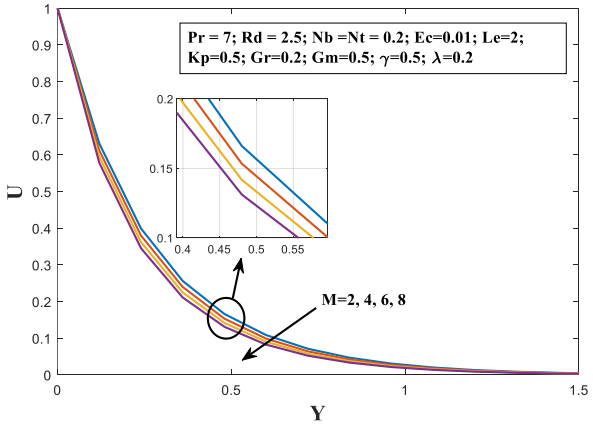

Figure 3. Velocity profile for different values of M.

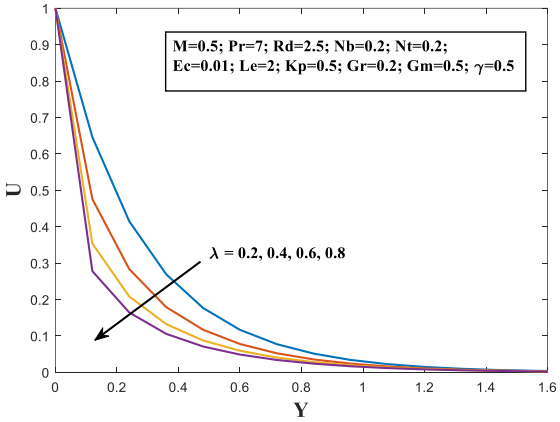

Figure 4. Velocity profile for different values of λ.

The changes in velocity for various values of M are shown in Figure 3. It is seen here that the velocity of the nanofluid decreases as the magnetic parameter rises. As the magnetic field parameter increases, a resistive force called a Lorentz force is produced, which retards the magnetic pressure drop affecting the velocity. As a result, the motion gets slowed down. Therefore, the velocity decreases with the increasing value of M. Figure 4 depicts the influence of the Williamson parameter on the velocity profile. A decreasing behavior is observed for velocity with the increase of λ.

It can be observed in Figures 5 and 6 as Nt rises, both the temperature and nanoparticle concentration profile increase. The increase in Nt may be explained by an increase in the thermophoresis force, which causes nanoparticles to migrate more swiftly from the hot surface to the cool surface, away from the sheet. Because the nanoparticles return from the hotter

surface, the temperature inside the boundary layer region rises. In addition, the concentration profile increases because of the motion of the nanoparticles due to the thermophoresis force.

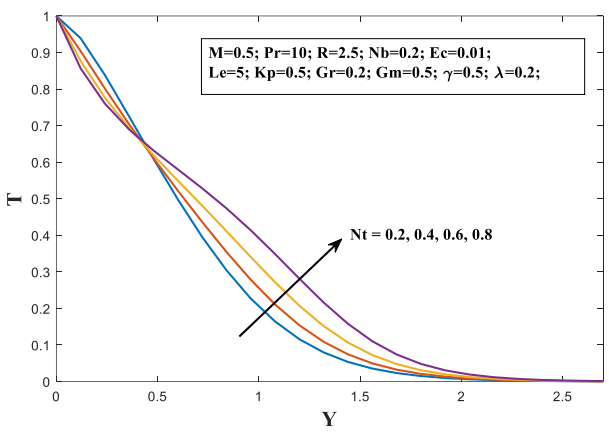

Figure 5. Temperature profile for different values of Nt

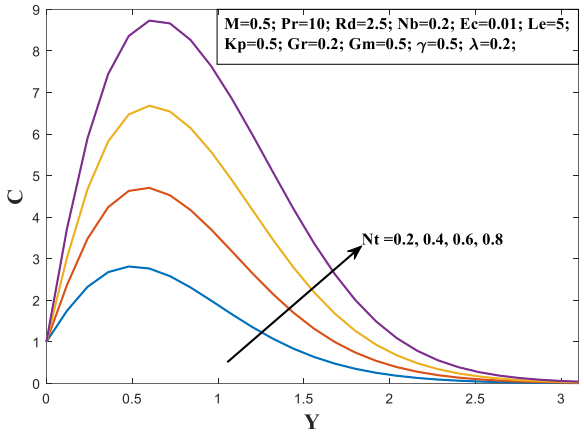

Figure 6. Concentration profile for different values of Nt.

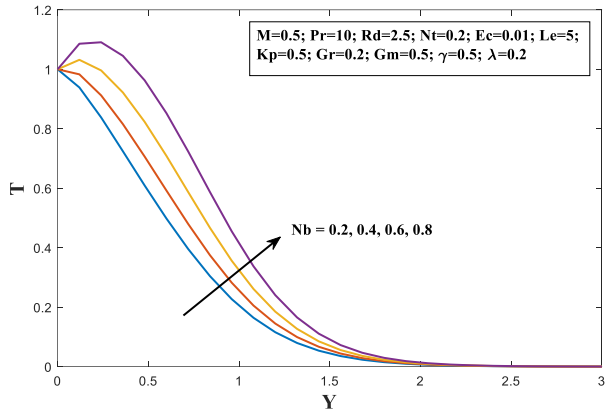

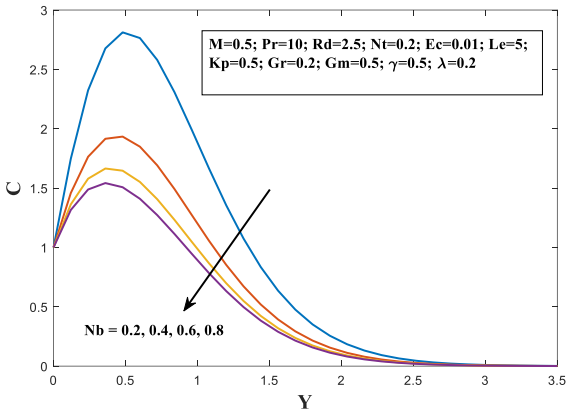

Figure 7. Temperature profile for different values of Nb. **Figure 8.** Concentration profile for different values of Nb.

The effect of Nb on temperature is seen in Figure 7. From the graph, it's clear that as Nb increases, so does the temperature. It is commonly known that collisions between nanoparticles increase with Nb because Nb causes nanoparticles to move more randomly. In consequence, the temperature inside the boundary layer increases as the kinetic energy is converted into thermal energy. Conversely, the concentration profile decreases with increasing Nb, as seen in Figure 8, which displays the concentration profile for various values of Nb. The reason is when Nb grows, particles prefer to cluster closer together.

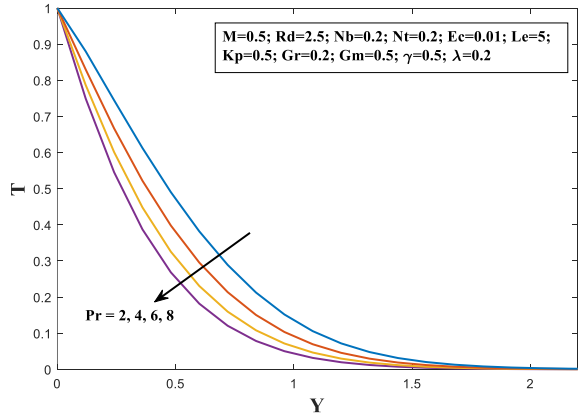

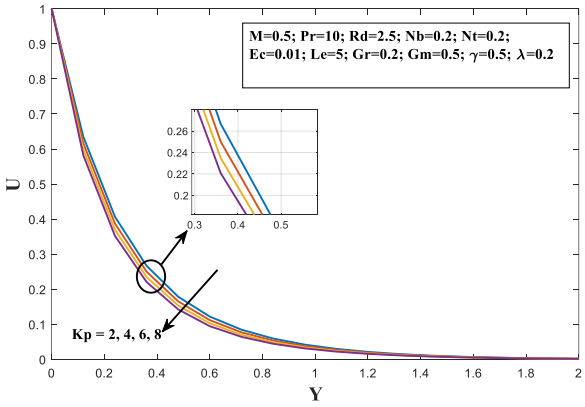

Figure 9. Temperature profile for different values of Pr. **Figure 10.** Velocity profile for different values of Kp.

Figure 9 exhibits the effect of Pr on dimensionless temperature, respectively. As Pr rises, it's easy to see how the temperature within the boundary layer area drops. Momentum

diffusivity to temperature diffusivity is the basis for the concept of Pr. So, a high Prandtl number indicates poor thermal conductivity and a smaller thermal layer structure since momentum diffuses more quickly than heat. As the Prandtl number rises, the heat transfer rate of the fluid rises, causing the temperature of the boundary layer to fall. Figure 10 reveals the impact of K_p on the velocity profile. It is clear from the figure that the velocity decreases with the increase in K_p. This occurs because an enhancement in Kp amplifies the porous layer, and thus, velocity in the boundary layer decreases.

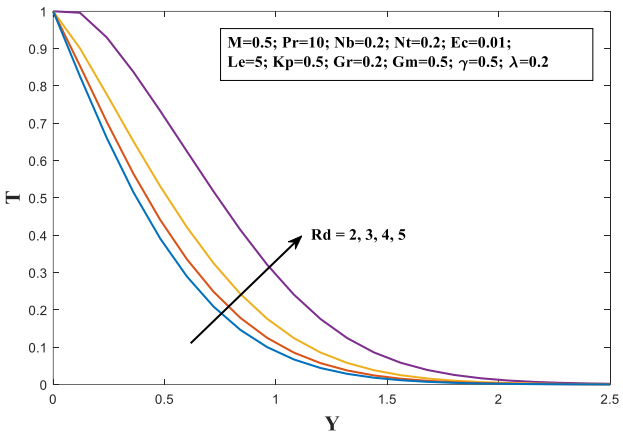

Figure 11. Temperature profile for different values of Rd.

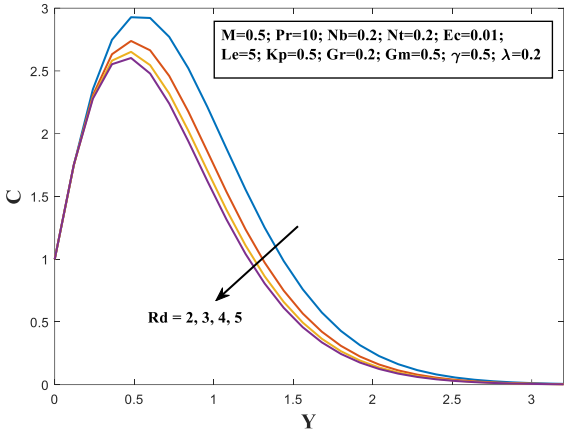

Figure 12. Concentration profile for different values of Rd.

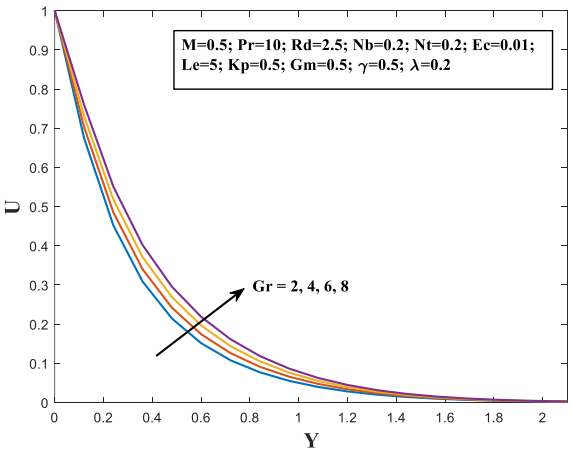

Figure 13. Velocity profile for different values of Gr.

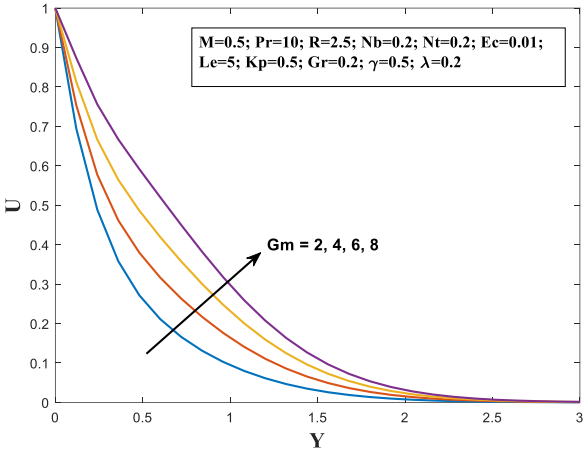

Figure 14. Velocity profile for different values of Gm.

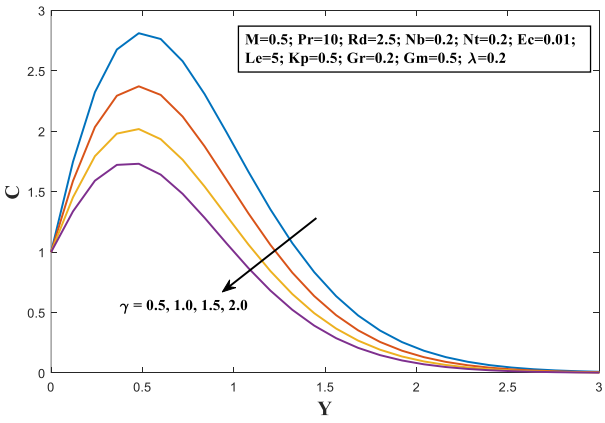

Figure 15. Concentration profile for different values of γ.

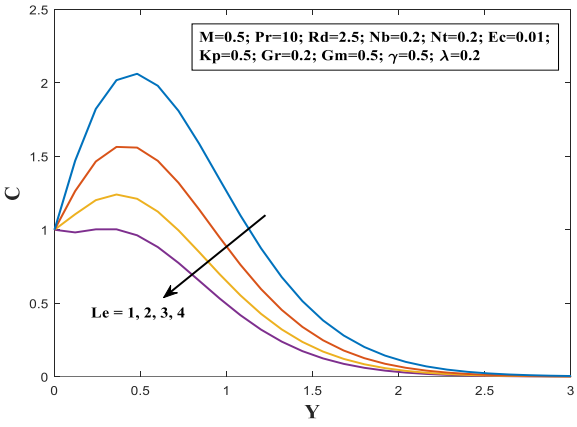

Figure 16. Concentration profile for different values of Le.

Figure 11 and 12 shows the influence of radiation parameter on the temperature profile and concentration profile, respectively. It can be seen that the temperature increases with the increase in the value of radiation parameters, whereas the opposite trend is seen in the case of nanoparticle concentration. That's because we're seeing the result of heat energy being released

into the fluid due to an increase in thermal radiation. Figures 13 and 14 depicted the impact of the Grashof number and modified Grashof number on the velocity profile. It is clear from the graph that the velocity profile increases with the increase in both parameters. As the Grashof number represents the ratio of buoyant force to viscous force, this makes sense. In physical terms, a high Grashof number indicates rapid fluid motion due to a large buoyant force. The impact of the changed Grashof number on the velocity profile may be understood similarly.

Figure 15 illustrates how the chemical reaction parameter (γ) affected the concentration of nanoparticles. The graph clearly shows that fewer nanoparticles are present at the surface when we raise the reaction parameter. The fundamental cause is that when a chemical reaction parameter's value rises, so does the number of solute molecules engaged in the reaction. As a result, the concentration profile declines. Thus, using several chemical processes results in considerable depletion of the solutal boundary layer, which increases mass transport phenomena.

Lastly, Figure 16 shows the concentration profile for the Lewis number (Le), and it can be seen that the concentration profile decreases gradually with the increase in Lewis number (Le). We know that the rate of mass transfer increases with the increase in Lewis number. As a result, the nanoparticle volume fraction decreases near the boundary as the value of the Lewis number increases.

To verify the validity of our numerical technique, Table 1 compares our obtained findings qualitatively to those of earlier published studies. It can be seen that the results are in excellent agreement.

Table 1. Comparison of the accuracy of the present results with the previous results of Bég et al. [43], *Khan et al.* [42] *and Rao and Deka* [26]

Increased Parameter	*Bég et al.* [36]			*Khan et al.* [19]			*Rao and Deka* [23]			***Present study***		
	U	$\bar{T}$	$\bar{C}$	U	$\bar{T}$	$\bar{C}$	U	$\bar{T}$	$\bar{C}$	$\boldsymbol{U}$	$\boldsymbol{\bar{T}}$	$\boldsymbol{\bar{C}}$
M							*Dec*	*Inc*		***Dec***		
Nt	*Inc*	*Inc*						*Inc*	*Inc*		***Inc***	***Inc***
Nb	*Inc*	*Inc*			*Inc*	*Dec*		*Inc*	*Dec*		***Inc***	***Dec***
Pr		*Dec*			*Dec*			*Dec*	*Dec*		***Dec***	
R	*Dec*				*Inc*	*Dec*		*Inc*			***Inc***	***Dec***
Le						*Dec*			*Dec*			***Dec***
γ									*Dec*			***Dec***
Gr	*Inc*						*Inc*			***Inc***		
Gm	*Inc*						*Inc*			***Inc***		

6. Conclusions

The heat and mass transfer of the two-dimensional unsteady MHD flow of a Williamson nanofluid over a porous vertical moving cylinder is studied and analyzed in this article. An explicit finite difference scheme is utilized to solve the non-linear governing equations and obtain the numerical results. The findings are classified as below-

In the boundary layer area, the nanofluid's velocity decreases when the magnetic parameter, Williamson parameter, and permeability parameter are increased, whereas the reverse trend is seen as the Grashof number and modified Grashof number are raised.

Increases in the thermophoresis, Brownian motion, and radiation parameters all lead to a higher temperature profile for the nanofluid, whereas increases in the Prandtl number have the opposite effect.

The volume fraction of nanoparticles inside the boundary layer area rises as the thermophoretic effect grows but begins to decrease as the chemical reaction parameter, Brownian motion parameter, radiation parameter, and Lewis number increase in value.

This research presents an efficient Williamson nanofluid model for heat and mass transmission, and so has applications in the industrial cooling industry and the nuclear reactor.

Funding

This research received no external funding

Acknowledgments

The authors are thankful to the unknown reviewers for their valuable suggestions and critical comments on our original manuscript.

Conflicts of Interest

The authors declare no conflict of interest.

Nomenclature

t	time (s)
x, r	cylindrical coordinates tangential to the surface and along the radial direction, respectively (m)
X, R	dimensionless cylindrical coordinates along the surface and along the radial direction, respectively
u, v	velocity components along x-axis and r-axis respectively (m s^{-1})
U, V	dimensionless velocity components along x-axis and r-axis respectively
$\bar{T}$	temperature (K)
$\bar{C}$	nanoparticle concentration (mol L^{-1})
T	dimensionless temperature
C	dimensionless nanoparticle concentration
B_o	magnetic field strength (T)
S	Cauchy stress tensor
p	pressure
I	unit tensor
A_1	Rivlin-Erickson tensor
g	acceleration due to gravity (m s^{-2})
k_o	porous term (m^2)
C_p	specific heat at constant pressure (J kg^{-1} K^{-1})
D_B, D_T	co-efficient of Brownian and thermophoretic diffusion, respectively (m^2 s^{-1})
q_r	radiative heat flux
k^*	mean absorption coefficient
K_1	reaction coefficient
M	magnetic parameter
G_r	Grashof number
G_m	modified Grashof number
K_p	permeability parameter
E_c	Eckert number
Pr	Prandtl number
Rd	Radiation parameter
Nb	Brownian motion parameter
Nt	thermophoresis parameter
Le	Lewis number

Greek Symbols:

τ	dimensional time variable
ν	kinematic viscosity ($m^2 s^{-1}$)
$\bar{\tau}$	extra stress tensor
μ_o	limiting viscosity at zero stress rate
μ_∞	limiting viscosity at an infinite shear stress rate
Γ	Williamson co-efficient
σ_e	electrically conductivity ($S\ m^{-1}$)
ρ	density ($kg\ m^{-3}$)
β_t	coefficient of thermal expansion
β_c	co-efficient of concentration expansion
κ	thermal conductivity of the fluid
α	thermal diffusivity ($m^2 s^{-1}$)
λ	Williamson parameter
τ^*	the ratio between the effective heat capacity of nanoparticles to the effective heat capacity of base fluid
σ^*	Stefan-Boltzmann coefficient
γ	chemical reaction parameter

***Suffix*:**

w	at wall
∞	at free stream region.

References

1. Choi, S.U.S.; Eastman, J.A. Enhancing thermal conductivity of fluids with nanoparticles. *Proceeding of ASME International Mechanical Engineering Congress and Exposition*, **1995**, *66*, 99–105, https://www.osti.gov/biblio/196525.
2. Lee, S.; Choi, S.U.S.; Li, S.; Eastman, J.A. Measuring Thermal Conductivity of Fluids Containing Oxide Nanoparticles. *ASME. J. Heat Transfer*, **1999**, *121*, 280–289, https://doi.org/10.1115/1.2825978
3. Choi, S.U.S.; Li, S.; Yu, W.; Thompson, L.J. Anomalously increased effective thermal conductivities of ethylene glycol-based nanofluids containing copper nanoparticles. *Applied Physics Letters*, **2001**, *78*, 718–720, https://doi.org/10.1063/1.1341218.
4. Buongiorno, J. Convective transport in nanofluids. *Journal of Heat Transfer*, **2006**, *128*, 240–250, https://doi.org/10.1115/1.2150834.
5. Kuznetsov, A.V.; Nield, D.A. Natural convective boundary-layer flow of a nanofluid past a vertical plate. *International Journal of Thermal Sciences*, **2010**, *49*, 243–247, https://doi.org/10.1016/j.ijthermalsci.2009.07.015.
6. Khan, W.A.; Pop, I. Boundary-layer flow of a nanofluid past a stretching sheet. *International Journal of Heat and Mass Transfer*, **2010**, *53*, 2477–2483, https://doi.org/10.1016/j.ijheatmasstransfer.2010.01.032.
7. Makinde, O.D.; Aziz, A. Boundary layer flow of a nanofluid past a stretching sheet with a convective boundary condition. *International Journal of Thermal Sciences*, **2011**, *50*, 1326–1332, https://doi.org/10.1016/j.ijthermalsci.2011.02.019.
8. Rana, P.; Bhargava, R. Flow and heat transfer of a nanofluid over a non-linearly stretching sheet: A numerical study. *Communications in Nonlinear Science and Numerical Simulation*, **2012**, *17*, 212–226, https://doi.org/10.1016/j.cnsns.2011.05.009.
9. Williamson, R.V. The flow of pseudoplastic materials. *Industrial and Engineering Chemistry*, **1929**, *21*, 1108–1111, https://doi.org/10.1021/ie50239a035.
10. Subbarayudu, K.; Suneetha, S.; Reddy, P.B.A. The assessment of time dependent flow of Williamson fluid with radiative blood flow against a wedge. *Propulsion and Power Research*, **2020**, *9*, 87–99, https://doi.org/10.1016/j.jppr.2019.07.001.
11. Lyubimova, T.P.; Perminov, A.V.; Kazimardanov, M.G. Stability of quasi-equilibrium states and supercritical regimes of thermal vibrational convection of a Williamson fluid in zero gravity conditions. *International Journal of Heat and Mass Transfer*, **2019**, *129*, 406–414, https://doi.org/10.1016/j.ijheatmasstransfer.2018.09.112.

12. Hashim, M.A.; Hamid, A.; Khan, M. Multiple solutions for MHD transient flow of Williamson nanofluids with convective heat transport. *Journal of the Taiwan Institute of Chemical Engineers*, **2019**, *103*, 126–137, https://doi.org/10.1016/j.jtice.2019.07.001.
13. Hamid, A.; Hashim, M.A.; Khan, M.; Alshomrani, A.S. An investigation of thermal and solutal stratification effects on mixed convection flow and heat transfer of Williamson nanofluid. *Journal of Molecular Liquids*, **2019**, *284*, 307–315, https://doi.org/10.1016/j.molliq.2019.03.181.
14. Khan, M.; Malik, M.; Salahuddin, T.; Hussian, A. Heat and mass transfer of Williamson nanofluid flow yield by an inclined Lorentz force over a non-linear stretching sheet. *Results Phys.*, **2018**, *8*, 862–868, https://doi.org/10.1016/j.rinp.20 18.01.005.
15. Megahed, A.M. Williamson fluid flow due to a non-linearly stretching sheet with viscous dissipation and thermal radiation. *J. Egypt. Math. Soc.*, **2019,** *27*, 12, https://doi.org/10.1186/s42787-019-0016-y.
16. Bouslimi, J.; Omri, M.; Mohamed, R.A.; Mahmoud, K.H.; Abo-Dahab, S.M.; Soliman, M.S. MHD Williamson Nanofluid Flow over a Stretching Sheet through a Porous Medium under Effects of Joule Heating, Nonlinear Thermal Radiation, Heat Generation/Absorption, and Chemical Reaction. *Adv. Math. Phys.*, **2021**, *2021*, 9950993, https://doi.org/10.1155/2021/9950993.
17. Gupta, S.; Kumar, D.; Singh, J.: Analytical study for MHD flow of Williamson nanofluid with the effects of variable thickness, non-linear thermal radiation and improved Fourier's and Fick's Laws. *SN Appl. Sci.*, **2020**, *2*, 438, https://doi.org/10.1007/s42452-020-1995-x.
18. Sharafat, A.; Zahoor, R.M.A.; Nawaz, C.T.; Iftikhar, A.; Numan, M.; Muhammad, S. Analysis of Williamson nanofluid with velocity and thermal slips past over a stretching sheet by Lobatto IIIA numerically. *Thermal Science*, **2021**, *4(A)*, 2795-2805, https://doi.org/10.2298/TSCI200620159A.
19. Kumaran, G.; Sivaraj, R. Non-linear thermal radiation effect on magnetohydrodynamic williamson nanofluid past a wedge/flat plate/stagnation point of the plate with activation energy, *Computational Thermal Sciences: An International Journal*, **2021,** *13(5)*, 61-81. https://doi.org/10.1615/ComputThermalScien.2021037808.
20. Abbas, A.; Jeelani, M.B.; Alnahdi, A.S.; Ilyas, A. MHD Williamson Nanofluid Fluid Flow and Heat Transfer Past a Non-Linear Stretching Sheet Implanted in a Porous Medium: Effects of Heat Generation and Viscous Dissipation. Processes **2022**, 10, 1221. https://doi.org/10.3390/pr10061221.
21. England, W.G.; Emery, A.F. Thermal Radiation Effects on the Laminar Free Convection Boundary Layer of an Absorbing Gas. *ASME. J. Heat Transfer.*, **1969**, *91*, 37–44, https://doi.org/10.1115/1.3580116.
22. Khan, M.S.; Alam, M.M.; Tzirtzilakis, E.E.; Ferdows M.; Karim, I. Finite difference simulation of MHD radiative flow of a nanofluid past a stretching sheet with stability analysis. *Int. J. Adv. Thermofluid Res.*, **2016**, *2*, 31–46, http://econ.uop.gr/~etzirtzilakis/Papers/26.pdf.
23. Kumar, M. A.; Reddy, Y. D.; Rao, V. S.; Goud, B. S. Thermal radiation impact on MHD heat transfer natural convective nano fluid flow over an impulsively started vertical plate. *Case Studies in Thermal Engineering*, **2021**, *24*, 100826, https://doi.org/10.1016/j.csite.2020.100826.
24. Ali, A.; Kanwal, T.; Awais, M.; Shah, Z.; Kumam, P.; Thounthong, P. Impact of thermal radiation and non-uniform heat flux on MHD hybrid nanofluid along a stretching cylinder. *Scientific reports*, **2021**, *11*, 20262, https://doi.org/10.1038/s41598-021-99800-0.
25. Lv, Y.P.; Shaheen, N.; Ramzan, M.; Mursaleen, M.; Nisar, K. S.; Malik, M.Y. Chemical reaction and thermal radiation impact on a nanofluid flow in a rotating channel with Hall current. *Scientific Reports*, **2021**, *11*, 19747, https://doi.org/10.1038/s41598-021-99214-y.
26. Rao, S.; Deka, P. A numerical solution using EFDM for unsteady MHD radiative Casson nanofluid flow over a porous stretching sheet with stability analysis. *Heat Transfer*, **2022**, 1-23, https://doi.org/10.1002/htj.22679.
27. Ramzan, M.; Farooq, M.; Hayat, T.; Chunge, J.D. Radiative and Joule heating effects in the MHD flow of a micropolar fluid with partial slip and convective boundary condition, *Journal of Molecular Liquids*, **2016**, *221*, 394–400, https://doi.org/10.1016/j.molliq.2016.05.091.
28. Rasheed, H.U.; AL-Zubaidi, A.; Islam, S.; Saleem, S.; Khan, Z.; Khan, W. Effects of Joule Heating and Viscous Dissipation on Magnetohydrodynamic Boundary Layer Flow of Jeffrey Nanofluid Over a Vertically Stretching Cylinder. *Coatings*, **2021**, *11*, 353, https://doi.org/10.3390/coatings11030353.
29. Shafiq, A; Khan, M.N.; Nadeem, S.; Rehman, A.; Ahmad, H.; Ali, R. Impact of Joule heating and multiple slips on a Maxwell nanofluid flow past a slendering surface, *Commun. Theor. Phys.*, **2022**, *74*, 015001, https://doi.org/10.1088/1572-9494/ac3bc8.
30. Khan, M.R.; Abidi, A.; Madiouli, J.; Guedri, K.; Al-Bugami, A.M.; Al-arabi, T.H.; Al-Zhour, Z.; Galal, A.M. Impact of Joule heating and viscous dissipation on magnetohydrodynamics boundary layer flow of viscous

nanofluid subject to the stretched surface. *Journal of Process Mechanical Engineering*, **2021**, https://doi.org/10.1177/09544089211064120.
31. Gopalakrishnan, K.S.; Oyelakin, I.S.; Mondal, S.; Sharma, R.P. Impact of Joule heating and non-linear thermal radiation on the flow of Casson nanofluid with entropy generation, *International Journal of Ambient Energy*, **2021**, https://doi.org/10.1080/01430750.2021.1973559.
32. Mahanthesh, B.; Shehzad, S.A.; Ambreen, T.; Khan, S.U. Significance of Joule heating and viscous heating on heat transport of MoS2–Ag hybrid nanofluid past an isothermal wedge. *J Therm Anal Calorim* **2021**, *143*, 1221–1229. https://doi.org/10.1007/s10973-020-09578-y.
33. Naveed, M.; Ali, S.; Hasnain, J.; Abbas, Z. Analysis of the effect of joule heating and hall current on flow of hybrid nanofluid over a curved stretching surface with melting boundary condition. *Heat Transfer Research*, **2021**, *52*, 1-16, https://doi.org/10.1615/HeatTransRes.2021036278.
34. Khan, M.R.; Mao, S.; Deebani, W.; Elsiddieg, A.M.A. Numerical analysis of heat transfer and friction drag relating to the effect of Joule heating, viscous dissipation and heat generation/absorption in aligned MHD slip flow of a nanofluid. *Int Commun Heat Mass Transfer*, **2022**, *131*, 105843, https://doi.org/10.1016/j.icheatmasstransfer.2021.105843.
35. Irfan, M.; Nadeem, A.; Nasir, N.; Waqas, M.; Khan, W.A. Thermal phenomenon of Joule heating in the radiative flow of Carreau nanofluid. *Pramana - J Phys*, **2022,** *96*, 90, https://doi.org/10.1007/s12043-022-02327-w.
36. Pai, S.I. Viscous Flow Theory: Vol. 1. Laminar Flow. *D.VanNostrand Co. New York, USA*, **1956**, https://www.amazon.com/Viscous-Flow-Theory-I-Laminar/dp/B000E5WOLO.
37. Schlichting, H. Boundary Layer Theory. *McGraw-Hill. 6, New York*, **1964**.
38. Kuznetsov, A.V.; Nield, D.A. Natural convective boundary-layer flow of a nanofluid past a vertical plate. *International Journal of Thermal* Sciences, **2010**, *49*, 243–247, https://doi.org/10.1016/j.ijthermalsci.2009.07.015.
39. Brewster, M.Q. Thermal radiative transfer properties. *John Wiley and Sons. New York*, **1972**.
40. Sparrow, E.M.; Cess, R.D. Radiation heat transfer. *Washington: Hemisphere*, **1978**.
41. Raptis, A. Radiation and free convection flow through a porous medium. *Int Commun Heat Mass Transf.*, **1998**, *25*, 289–95, https://doi.org/10.1016/S0735-1933(98)00016-5.
42. Khan, M.S.; Wahiduzzaman, M.; Uddin, M.S.; Sazad, M.A.K. Finite difference solution of MHD free convection heat and mass transfer flow of a nanofluid along a stretching sheet with heat generation effects. *Indian J. Theor. Phys.*, **2012**, *60*, 285–306, https://www.researchgate.net/publication/259961790_Finite_difference_solution_of_MHD_free_convection_heat_and_mass_transfer_flow_of_a_nanofluid_along_a_stretching_sheet_with_heat_generation_effects.
43. Bég, O.A.; Khan, M.S.; Karim, I.; Md. Alam, M.; Ferdows, M. Explicit numerical study of unsteady hydromagnetic mixed convective nanofluid flow from an exponentially stretching sheet in porous media. *Appl Nanosci*, **2014**, *4*, 943–957, https://doi.org/10.1007/s13204-013-0275-0.